Experimental Cell Research 372 (2018) 25–34

Contents lists available at ScienceDirect

Experimental Cell Research

journal homepage: www.elsevier.com/locate/yexcr

Matrix mineralization controls gene expression in osteoblastic cells

Johannes Wischmann[a], Florian Lenze[a], Antonia Thiel[a], Sakina Bookbinder[b], William Querido[b], Oxana Schmidt[c], Rainer Burgkart[a], Rüdiger von Eisenhart-Rothe[a], Günther H.S. Richter[c], Nancy Pleshko[b], Philipp Mayer-Kuckuk[a,*]

[a] Department of Orthopedics, Klinikum rechts der Isar, Technical University Munich, 81675 Munich, Germany
[b] Department of Bioengineering, Temple University, Philadelphia, PA 19122, USA
[c] Children's Cancer Research Center, Comprehensive Cancer Center Munich, German Translational Cancer Research Consortium and Department of Pediatrics, Klinikum rechts der Isar, Technical University Munich, 81675 Munich, Germany

ARTICLE INFO

Keywords:
Bone
Bone mineral
Bone matrix
Osteoblast
Gene Regulation

ABSTRACT

Osteoblasts are adherent cells, and under physiological conditions they attach to both mineralized and non-mineralized osseous surfaces. However, how exactly osteoblasts respond to these different osseous surfaces is largely unknown. Our hypothesis was that the state of matrix mineralization provides a functional signal to osteoblasts. To assess the osteoblast response to mineralized compared to demineralized osseous surfaces, we developed and validated a novel tissue surface model. We demonstrated that with the exception of the absence of mineral, the mineralized and demineralized surfaces were similar in molecular composition as determined, for example, by collagen content and maturity. Subsequently, we used the human osteoblastic cell line MG63 in combination with genome-wide gene set enrichment analysis (GSEA) to record and compare the gene expression signatures on mineralized and demineralized surfaces. Assessment of the 5 most significant gene sets showed on mineralized surfaces an enrichment exclusively of genes sets linked to protein synthesis, while on the demineralized surfaces 3 of the 5 enriched gene sets were associated with the matrix. Focusing on these three gene sets, we observed not only the expected structural components of the bone matrix, but also gene products, such as HMCN1 or NID2, that are likely to act as temporal migration guides. Together, these findings suggest that in osteoblasts mineralized and demineralized osseous surfaces favor intracellular protein production and matrix formation, respectively. Further, they demonstrate that the mineralization state of bone independently controls gene expression in osteoblastic cells.

1. Introduction

Osteoblasts are the sole bone-forming cells of the body [1]. They have the capacity for production of both the organic collagen matrix of bone, i.e. osteoid, and the subsequent mineralization of the matrix. In adult bone, the mineralized osseous surface is largely occupied by resting osteoblasts called bone-lining cells [2], while at areas of active bone formation, such as the bone multinuclear unit (BMU) or sites of bone repair, osteoblasts are attached to resorbed bone surfaces or osteoid [3]. Further, at sites where osteoblasts facilitate or completed mineralization, they are also observed on mineralized bone surfaces [3]. Together, osteoblasts reside on both mineralized and non-mineralized osseous surfaces, and are likely to transition between these two osseous surfaces.

The biological response of osteoblasts to these surfaces is only partly understood. With respect to mineralized surfaces, previous work showed that the collagen fibrils in mineralized bone contain a substituted calcium hydroxyapatite mineral [4,5], both inside and on their surface [6]. However, if and how the mineral influences osteoblast behavior remains largely elusive. In comparison to mineralized surfaces, more is known about the interaction of osteoblasts with non-mineralized matrix surfaces. Osteoblasts utilize focal adhesions for matrix recognition and binding via the extracellular domains of cell-membrane-spanning integrin receptors, particularly the β_1 integrin subunit [7]. This subunit forms a number of heterodimeric receptors, including $\alpha_{1-5}\beta_1$ and $\alpha_v\beta_{1,\,3,\,5}$ [8,9], and its functional relevance of the β_1 integrin subunit has been demonstrated in mouse models in vivo [10,11]. The heterodimeric integrin receptors on osteoblasts are capable of binding to the major components of bone matrix, such as type I collagen and non-collagenous matrix components including bone sialoprotein, osteopontin, or vitronectin [7]. Beyond attachment, matrix components such as type I collagen or fibronectin, although

* Corresponding author. Present address: Institute of Experimental Genetics, Helmholtz Center Munich, Ingolstaedter Landstr. 1, 85764 Neuherberg, Germany.
E-mail address: philipp.mayer-kuckuk@helmholtz-muenchen.de (P. Mayer-Kuckuk).

https://doi.org/10.1016/j.yexcr.2018.09.005
Received 17 May 2018; Received in revised form 21 August 2018; Accepted 4 September 2018
Available online 05 September 2018
0014-4827/ © 2018 The Authors. Published by Elsevier Inc. This is an open access article under the CC BY-NC-ND license (http://creativecommons.org/licenses/BY-NC-ND/4.0/).

immobilized within a ridged matrix, can also be recognized by osteoblasts as chemoattractants and induce haptotaxis, i.e. migration along a gradient of cellular adhesion sites or substrate-bound chemoattractants [12]. Notably, receptors such as integrin receptors play an important role as transducers, connecting matrix ligands to intracellular signaling pathways [13]. This suggests that matrix mineralization, for example simply by masking matrix components, could have a potentially significant effect on osteoblast function. Therefore, we hypothesized for this study that the state of matrix mineralization provides a functional signal to osteoblasts. In the absence of a suitable tissue surface model, we devised a surface model that provides either a mineralized or demineralized endogenous bone surface for the attachment of human osteoblastic cells, while maintaining matrix composition. Using this assay in combination with GSEA generated data demonstrating that bone matrix mineralization directly controls osteoblast biology.

2. Materials and methods

2.1. Chemicals and reagents

All chemicals were from Sigma (St. Louis, MO) unless noted otherwise. Ethylenediamine tetraacetic acid disodium salt (EDTA) was from Carl Roth (Karlsruhe, Germany). Peracetic acid (PAA) solution was purchased from Bioxal SA (Chalon-sur-Saône, France), while Trizol was procured from Sigma (St. Louis, MO).

2.2. Preparation and validation of bone surfaces

Fresh porcine tibia was obtained from a Munich slaughterhouse and stored at − 80 °C. After thawing at room temperature (RT), surrounding tissue of the tibia was removed with a single use scalpel. Using a water-cooled EXAKT 300 CL band saw from EXAKT (Hamburg, Germany) at 560 m/min saw band velocity, porcine tibia was cut into slices of 600 µm thickness each. The slices were demineralized in 0.5 M EDTA (aqueous solution, adjusted to pH 7) for 16 h. Based on pilot studies determining the optimal concentration and time, antimicrobial treatment of bone was carried out with 2% PAA for 16 h, followed by a washing step with phosphate buffered saline for 16 h. After the washing step, the bone was directly processed.

2.3. Osteodensitometry

The mineralization state of the osseous surfaces preparations was assessed using dual energy X-ray absorption (DXA). To perform DXA on 5 mineralized and 5 demineralized samples, a Faxitron Ultrafocus (Faxitron Bioptics LCC, Tucson, AZ) in combination with Vision DXA Version 2.4.2 software was employed. Samples were placed at the 2x magnification stage and data acquired sequentially at 40 kV/0.28 mA and 80 kV/0.14 mA. Measures of bone mineral density (BMD) was obtained from region-of-interest (ROI) measures. ROIs were plotted along the periphery of each of the 10 samples visualized on the Bone Map image.

2.4. Fourier transform infrared (FTIR) spectroscopy

Intact mineralized and demineralized samples were analyzed by FTIR in attenuated total reflection (ATR) mode using a Thermo Scientific Nicolet iS5 FTIR Spectrometer, mounted with the iD7 ATR accessory with a diamond crystal. Briefly, samples were dried with absorbent tissue wipers, placed in close contact with the ATR crystal and spectra were collected with 4 cm^{-1} resolution and 32 co-added scans. ATR correction of the spectra were performed using the OMNIC software (Thermo Scientific, Waltham, MA). The Unscrambler X software (CAMO, Magnolia, TX) was used to obtain the second derivative spectra to reveal details of subtle and overlapping peaks. The integrated area of peaks of interest were obtained using ISys chemical imaging analysis software (Malvern, Columbia, MD). Specific wavenumber ranges were used for assessment of several components of the bone matrix [14]: phosphate from hydroxyapatite (900–1185 cm^{-1}, PO_4 antisymetric stretching vibration), amide I, reflecting total protein (1585–1720 cm^{-1}, C=O stretching vibration), collagen (1325–1355 cm^{-1}, side chain vibrations), and carbonate incorporated into the hydroxyapatite (855–890 cm^{-1} CO_3 bending vibration). The relative amount of mineral to protein content was assessed by the phosphate/amide I peak ratio, and relative collagen content by the collagen/amide I ratio. Collagen maturity was estimated based on the 1660/1690 ratio within the amide I peak after baseline correction from 1700 to 1600 cm^{-1} [14]. Six samples were analyzed for each group (mineralized and demineralized), with three spectra collected in different regions of each sample.

2.5. Cell culture

The human osteosarcoma cells MG63, Hos and Saos-2 were obtained from the American Type Culture Collection (Manassas, VA). MG63 and Hos cells were cultured in Dulbecco's modified Eagle's medium (DMEM), while Saos-2 cells were cultured in RPMI-Medium 1640. Cell culture media and supplements for the above cell lines were purchased from Gibco (Waltham, MA). All media were supplemented with 10% fetal bovine serum (FBS), 100 U/ml penicillin/100 µg/ml streptomycin, and 1% L-glutamine. Cells were maintained at 37 °C in a humidified 5% carbon dioxide atmosphere, and sub-cultured at a 1:5 ratio. Two lots (426,160 and 435,102) of primary human osteoblast (termed HOB1 and HOB2) were procured from Lonza (Basel, Switzerland) and cultured in OBM Basal Medium (Lonza), supplemented with SingleQuots (Lonza), at 37 °C in a humidified 5% carbon dioxide atmosphere. Sub-cultivation was carried out at 80% confluency, using the recommended ReagentPack (Lonza), following the manual´s instructions.

To study cells on mineralized or demineralized bone surfaces, cells were seeded onto the osseous surface at a density of 200,000 cells/cm^2 and cultivated for 72 h. For harvest, cells were mechanically removed using a cell scraper, and collected in their appropriate medium through centrifugation (500 *g* for 5 min at RT).

2.6. Staining with fluorescent dyes

To detect live cells on osseous surfaces, they were fluorescence-labeled, using the Vybrant (Invitrogen Molecular Probes, Eugene, OR) dye DiD (excitation and emission wavelength maxima of 644 nm and 665 nm, respectively). This dye specifically was shown to offer in MG63 cells high labeling efficiency and minimal toxicity when compared for example to GFP labeling [15]. Labeling was carried out in cell suspension following the manual´s instructions. Fluorescent MG63 cells were seeded onto the osseous surfaces at a density of 200,000 cells/cm^2 and incubated for 72 h.

Cell morphology was assessed on fixed cells by co-staining with Alexa Fluor 647 phalloidin (excitation and emission wavelength maxima of 650 nm and 668 nm, respectively) and 4′,6-diamidino-2-phenylindole (DAPI) dihydrochloride (excitation and emission wavelength maxima of 358 nm and 461 nm, respectively), both procured from Thermo Fisher Scientific. MG63 cells were seeded onto the osseous surfaces at a density of 200,000 cells/cm^2 and incubated for 72 h. Then, co-staining was carried out, following a standard staining protocol for adherent cells. Briefly, MG63 cells were fixed with 4% paraformaldehyde (PFA) for 30 min and permeabilized with 0.1% Triton X-100 for 30 min at RT. After that, the samples were incubated with Alexa Fluor 647 phalloidin (methanol stock) at a concentration of 165 nM for 60 min at RT. Subsequently, the samples were incubated with DAPI dihydrochloride at a concentration of 300 nM for 5 min at RT. Each of the above stainings was followed by two washing steps with PBS for 5 min at RT.

2.7. Immunofluorescence staining

To detect expression of HMCN1 in adherent MG63 cells on the protein level, indirect immunofluorescence staining of HMCN1 protein together with DAPI nucleic acid staining was employed. Unconjugated rabbit-derived HMCN1 polyclonal IgG antibody (Thermo Fisher Scientific) and labeled donkey anti-rabbit IgG antibody (Invitrogen), conjugated to Alexa Fluor 594 (excitation and emission wavelength maxima of 590 nm and 617 nm, respectively) were used as primary and secondary antibody, respectively. MG63 cells were seeded onto the osseous surfaces at a density of 200,000 cells/cm^2 and incubated for 72 h. After incubation, staining was carried out. Briefly, cells were fixed with 4% PFA for 30 min and incubated with 1% FBS blocking solution for 15 min at RT. Then, the samples were incubated with the primary antibody at a concentration of 10 µg/ml, diluted in PBS with 0.1% FBS, for 60 min at RT. This was followed by three wash steps with PBS, each for 5 min at RT. Subsequently, the samples were incubated with the secondary antibody at a concentration of 1 µg/ml, diluted in PBS with 0.1% FBS, for 60 min at RT. This was again followed by three wash steps with PBS, each for 5 min at RT. In a final step, the samples were incubated with 300 nM DAPI dihydrochloride for 5 min at RT, and then washed as described for the previous steps.

2.8. Fluorescence microscopy

A Z1-Observer (Carl Zeiss, Jena, Germany) with integrated cultivation system device was used to acquire images from DiD and immunofluorescent stained samples. Imaging on the Z1 was performed using #45 Texas Red and #49 DAPI filters, an AxioCamMR3 camera, and LD A-Plan 32×/0.40 Ph 1 and EC Plan-Neofluar 10×/0.30 Ph 1 objectives. Imaging of Alexa Fluor 647 phalloidin and DAPI co-stained samples was carried out using a Fluoview 1200 Laser Scanning Confocal Microscope (Olympus, Hamburg, Germany) equipped with an Olympus UPlanSApo 40 × 1.25 Oil immersion objective at 600 nm step size. Stacks of 17–18 images were collected. Images were processed in ImageJ using the smooth, remove outliers, and brightness/contrast functions.

2.9. RNA isolation

Cells were resuspended in Trizol. Total RNA was extracted using RNeasy Plus Mini Kit (Qiagen, Hilden, Germany), following the manual´s instructions, and stored at − 80 °C. The RNA integrity number (RIN) was measured for quality control. cDNA was synthesized using QuantiTect Reverse Transcription Kit (Qiagen), and stored at − 20 °C. To obtain one RNA sample, cells harvested from two surfaces were pooled. Four independent RNA samples were prepared for each osseous surface.

2.10. Gene expression analysis

Genome-wide expression was measured using the Affymetrix Human Gene 1.0 ST microarray (Thermo Fisher Scientific). To normalize the acquired data across the samples, robust multi-array average (RMA) normalization was employed. The previously reported GSEA software in the platform-independent version [16] together with the Molecular Signatures Database (MSigDB, Broad Institute) [17] was used to analyze expression data. Genome-wide expression profiles received in microarray analysis were determined as two classes, labeled as “mineralized” and “demineralized”. GSEA was carried out utilizing the C5 gene ontology (GO) gene sets (GO biological process, GO cellular component, GO molecular function) from the MSigDB as gene set database, containing 6166 gene sets in total. Only incorporating gene sets including more than 15 and less than 500 genes, 4865 gene sets were considered for analysis. A weighted scoring scheme was set for enrichment statistics. Null distribution was estimated by 1000 gene set permutations, randomly assigning genes to gene sets, without affecting the size of each gene set. Results were analyzed, respecting a Normalized Enrichment Score (NES), p-value and false discovery rate (FDR), to detect distinctions in genome-wide expression for the two defined classes.

2.11. Quantitative real-time PCR (QRT-PCR)

For QRT-PCR the QuantiTect SYBR Green PCR Kit (Qiagen) in combination with the StepOnePlus Real-Time PCR System (Applied Biosystems, Darmstadt, Germany) was employed. The following ten commercial primer sets QuantiTect Primer Assay (Qiagen) were used to detect targets of interest: HMCN1 (Hs_HMCN1_1_SG, Cat. no.: QT00011228), NID2 (Hs_NID2_1_SG, Cat. no.: QT00055258), ITGA2 (Hs_ITGA2_1_SG, Cat. no.: QT00086695), VCAN (Hs_VCAN_1_SG, Cat. no.: QT00064064), GAPDH (Hs_GAPDH_1_SG, Cat. no.: QT00079247) and ACTB (Hs_ACTB_1_SG, Cat. no.: QT00095431). Each target was amplified in a total reaction volume of 20 µl per well, containing 10 µl QuantiTect SYBR Green PCR Master Mix, 2 µl QuantiTect Primer, 2 µl cDNA and 6 µl RNase-free water. DNA amplification was initiated through an incubation step of 15 min at 95 °C, followed by 40 cycles of a 15 s denaturation step at 95 °C, a 30 s annealing step at 55 °C and a 30 s extension step at 72 °C. Relative gene expression analysis based on the comparative method (ΔΔCT method of relative quantification) was used, determining relative gene expression values of the mineralized phenotype as endogenous reference sample. Relative gene expression was measured, normalized to the corresponding values of the housekeeping genes (GAPDH and ACTB).

2.12. Statistical analyses

GraphPad Prism 7 was employed for statistical analyses. To compare mineralized to demineralized samples, an unpaired *t*-test was used. A p-value of less than 0.05 was considered significant. Statistical significance for GSEA results was defined for a p-value of less than 0.001 and a false discovery rate (FDR) of less than 0.005.

3. Results

3.1. Development and validation of a matrix mineralization model

To devise a model that provides an endogenous bone surface with different mineralization states, we selected porcine tibia as starting material. Surfaces with an area and thickness range in the cm and submm, respectively, were cut (Fig. 1A). Subsequently, a chelate-based demineralization was carried out and the degree of demineralization was assessed using X-ray techniques. Planar X-ray imaging visualized the mineralized but not demineralized surfaces (Fig. 1B). Using DXA analysis, an average BMD of 76.6 ± 17.6 g/cm^2 (n = 5) was measured for the mineralized surface, while BMD was undetected in the demineralized surfaces (Fig. 1C).

To compare the mineralized and demineralized surfaces on a molecular level, FTIR spectral analyses were employed. Fig. 2A shows the absorption spectra of the two surfaces. The mineral found in the mineralized surfaces was typical of bone apatite, with the contributions from phosphate and carbonate [14]. Comparable peaks were detected for amide I, II, and III, arising from protein components, as well as the collagen peak arising from side chain vibrations, in both mineralized and demineralized surfaces, while the peaks for phosphate and carbonate were only observed on the mineralized surfaces. Second derivative spectra were used to show the peaks in more detail, confirming the absence of mineral peaks in the demineralized surfaces (Fig. 2B). Quantitative analysis of the spectra shows the drastic reduction in the mineral content of the demineralized surfaces (Fig. 2C). In contrast, the collagen content (Fig. 2D) and the collagen maturity (Fig. 2E) were similar between the mineralized and demineralized surfaces. These

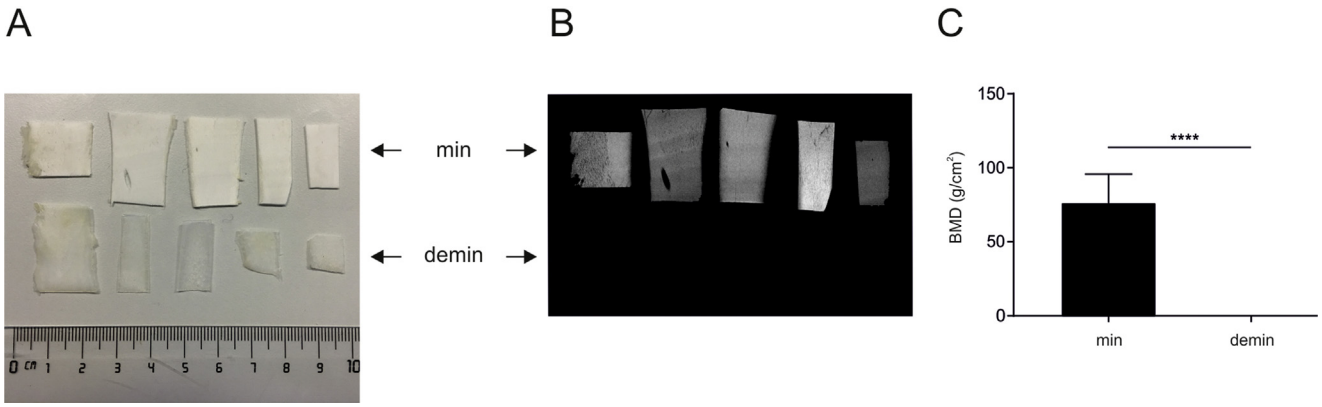

Fig. 1. *The surface model mimics mineralized and demineralized endogenous bone.* (**A**) Photographs of mineralized and demineralized bone surfaces prepared for subsequent cell seeding. (**B**) Planar X-ray images of mineralized (top row) and demineralized (bottom row) bone surfaces. (**C**) DXA measure of BMD. Means and standard deviation are shown. Significance was denoted as ****$p < 0.0001$. Abbreviations: demin, demineralized; min, mineralized.

results show that the demineralization of the surfaces was successful, leading to the complete removal of the mineral substance without affecting the integrity of the organic matrix.

To utilize the model for the study of cellular responses to the surface, we first monitored cell adherence to the surfaces. As endogenous bone surfaces lack optical transparency, osteoblastic cells were transiently labeled with a fluorescent dye. Forty-eight hours post seeding, cells on both the mineralized and demineralized surfaces showed normal cell morphology and formed uniform cell layers (Fig. 3A–D). Cytoskeletal F-actin staining further supported a comparable cell morphology on the mineralized and demineralized bone surfaces (Fig. 3E and F). The planar geometry of the osseous surfaces permitted complete recovery of the cells using gentle, mechanical means (Fig. 3G and H). This led to the separation of cells and surface, while offering sufficient cell harvest for subsequent molecular analysis.

3.2. Gene expression signatures on mineralized and demineralized surfaces

To offer a comprehensive and robust molecular analysis of the response of osteoblastic cells to osseous surfaces, we relied on standard gene expression profiling. For subsequent data analysis, GSEA was selected because it permits an initial broad view on the data, rather than

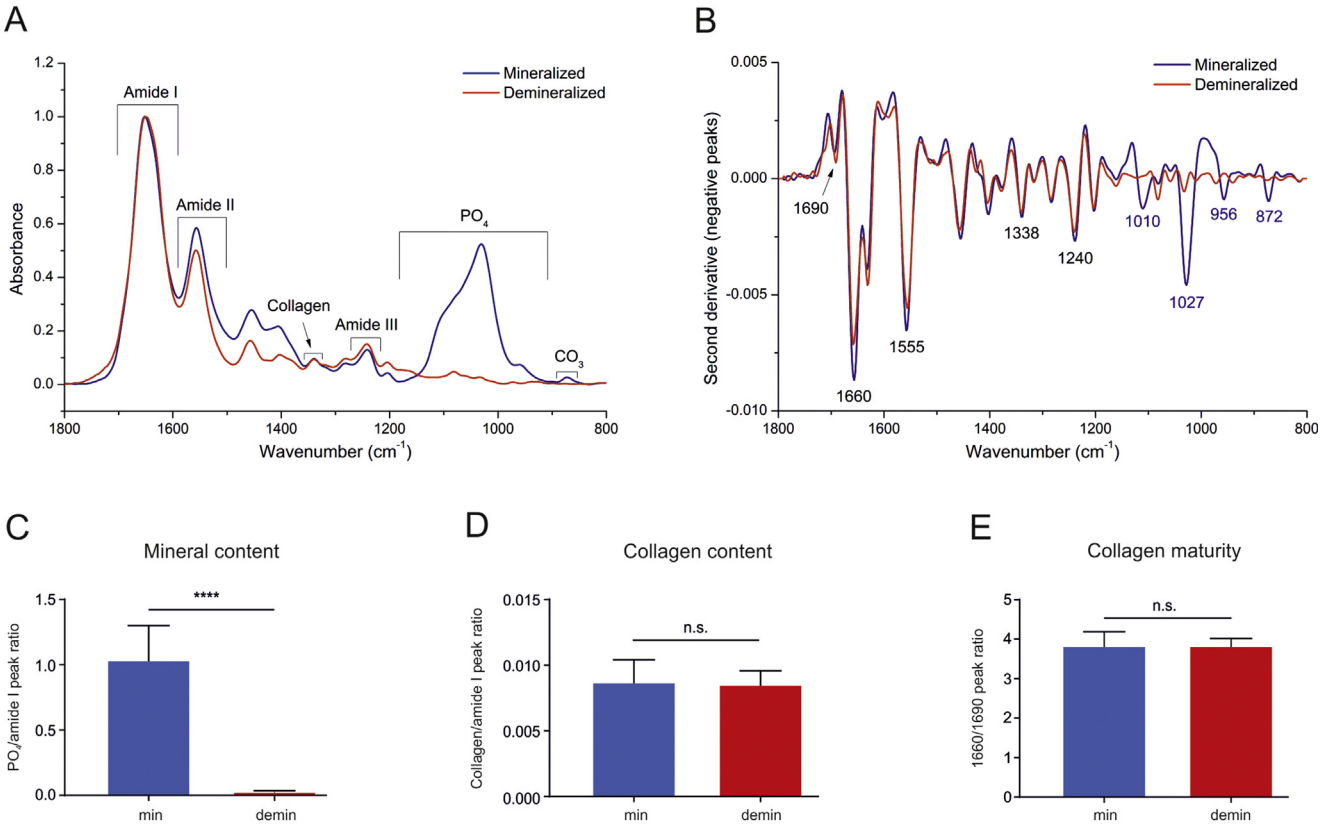

Fig. 2. *The mineralized and demineralized surfaces differ only in their mineralization state.* (**A**) Raw FTIR spectra show comparable peaks for amide I, II, and III (arising from total protein), and for collagen in both surfaces, while PO_4 and CO_3 peaks were only observed in the mineralized surface. (**B**) Second derivative spectra show more details of subtle and overlapping peaks, confirming the absence of mineral in the demineralized surface. (**C**) Relative mineral content (PO_4/amide I peak ratio) was significantly reduced in the demineralized surfaces. (**D**) Relative collagen content (collagen/amide I peak ratio) and (**E**) collagen maturity (1660/1690 peak ratio) were the same in mineralized and demineralized surfaces (n.s., not significant, ***$p < 0.001$). Abbreviations: demin, demineralized; min, mineralized.

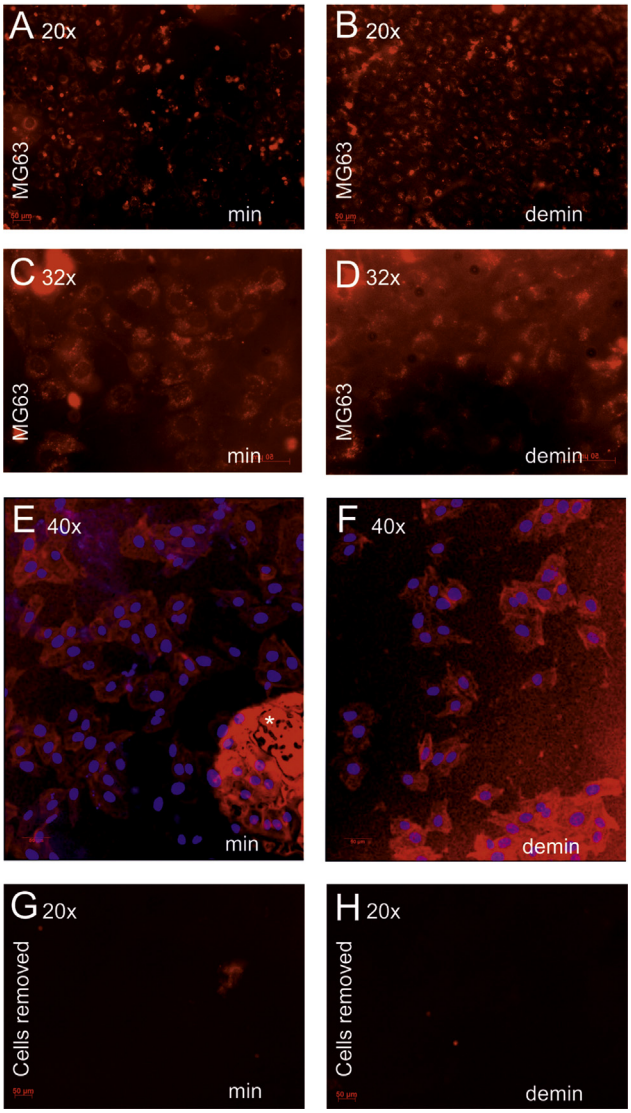

Fig. 3. *Normal gross attachment of osteoblastic cells on the mineralized and demineralized surfaces*. (**A–D**) MG63 cells marked with DiD (red channel) on mineralized (left images) and demineralized (right images) bone surfaces forty-eight hours post seeding at a density of 200,000 cells/cm^2. Cells show normal morphology and uniform cell attachment. Imaging was performed on live cells (**E** and **F**). Co-staining of MG63 cells with phalloidin (red channel) and DAPI (blue channel). Images taken on fixed cells. The white star marks an artifact from the bone tissue. (**G** and **H**) Osseous surfaces after mechanical cell-removal, illustrating almost complete cell removal. The image depicts the same ROI as shown in **A** and **B** prior to cell removal. Imaging was performed on live cells. Abbreviations: demin, demineralized; min, mineralized.

the need to select genes early in the analysis. Gene expression data was deposit for public access in GENE EXPRESSION OMNIBUS (GEO). The GSEA of 2735 gene sets found 839 and 1896 upregulated gene sets in osteoblastic cells on mineralized and demineralized surfaces, respectively (Fig. 4A). A subsequent assessment of the gene sets with highly significant upregulation showed similar distributions between the surfaces (Fig. 4B and C). Together, these findings suggested a profound impact of the mineralization state on the cellular response. We then identified the top 5 gene sets on mineralized and demineralized surfaces (Fig. 4D and E) and displayed enrichment profiles of the corresponding top gene sets with highest achieved Normalized Enrichment Scores (NES). Osteoblastic cells on the mineralized surface exclusively enriched gene sets associated with the ribosome or endoplasmic reticulum (ER) (Fig. 4D). In sharp contrast, the top 5 upregulated gene sets on the demineralized surface comprised three genes sets associated with the ECM and cell motility (Fig. 4E, bars with yellow outline), as well as two gene sets related to vascular development (Fig. 4E).

To further detail on the genes differentially regulated in osteoblastic cells on mineralized and demineralized bone surfaces, we mapped the genes of the GO EXTRACELLULAR MATRIX COMPONENT, GO PROTEIN COMPLEX INVOLVED IN CELL ADHESION, and GO EXTRACELLULAR STRUCTURE ORGANIZATION gene sets, which where stringently enriched in osteoblastic cells on the demineralized surface (Fig. 5A–C). Then, we surveyed whether these genes have a known or unknown function in osteoblasts (Suppl. Table). Of the 29 genes, 26 genes had a well-established (Fig. 5A–C, green bars) or at least reported (Fig. 5A–C, light green bars) function in osteoblasts. More importantly, we also observed enrichment of two matrix genes, HMCN1 and NID2 (Fig. 5A and C, purple bars), previously not recognized to be induced in osteoblasts. Lastly, we plotted the top 10 upregulated genes on both osseous surfaces and found AMTN, SERPINE1 and ITGA2 as genes within examined gene sets among the top 10 upregulated genes on the demineralized bone surface (Fig. 5D). Together, these findings (1) demonstrated that expression of many of the essential osteoblastic matrix genes was a sole function of the degree of bone surface mineralization, and (2) identified osteoblastic induction of HMCN1 and NID2 in response to demineralized surfaces. The latter, was confirmed by QRTPCR measures (Fig. 5E and F), using ITGA2 and VCAN (Fig. 5G and H) as positive controls. We note a higher induction of HMCN1 on demineralized bone when compared to NID2 (Fig. 5E and F). The cellular presence of HMCN1 protein was validated using an immunofluorescence technique. Cellular localization of HMCN1 was clearly shown (Fig. 5I), while images indicated extracellular HMCN1 (Fig. 5J).

To investigate the relevance of above findings further, expression of HMCN1, NID2, ITGA2 and VCAN was cross-validated in other osteoblastic cell types (Fig. 6). In addition to MG63 cells, the transformed cell lines Saos-2 and Hos as well as two independent batches of primary human osteoblasts (HOB1 and HOB2) were studied. HMCN1 was induced on demineralized surfaces in all cell types, yet a varying degrees (Fig. 6A). A particularly robust induction was observed in Saos-2 cells (Fig. 6A). Expression of NID2 differed among the transformed cell types (Fig. 6B), while a decrease in expression on demineralized bone was consistent between the HOB batches (Fig. 6B). In comparison, we measured expression of the VCAN and ITGA2 control genes. VCAN expression increased on the demineralized surface in all transformed cell types, but decreased in the primary HOB cells (Fig. 6C). Similarly, ITGA2 increased on the demineralized surface in all transformed cell types, yet at a higher magnitude than VCAN (Fig. 6C). In primary osteoblasts ITGA2 expression decreased on demineralized surfaces (Fig. 6D). Together, HMCN1 expression on demineralized surface stood out as it was (1) generally increased in osteoblastic cells, (2) increased in primary osteoblasts on demineralized surfaces, while the other three markers were decreased in these cells, and (3) showed the highest surface induced induction.

4. Discussion

We demonstrated here that the mineralization state of bone independently controls gene expression in osteoblastic cells, and thus confirmed our initial hypothesis. Mineralized and demineralized osseous surfaces favor intracellular protein production and matrix formation, respectively. Further, our experiments identified HMCN1 and NID2 as matrix proteins overexpressed by osteoblastic cells on demineralized bone. The discoveries above were made using a potentially valuable surface model that permits the investigation of osseous mineralization on cell function.

The surface model we devised is based on a planar endogenous bone surface, a surface previously used to study primarily osteoclasts, more recently for example assessing adhesion dynamics [18], but occasionally also osteoblasts [19]. The use of endogenous bone is an important

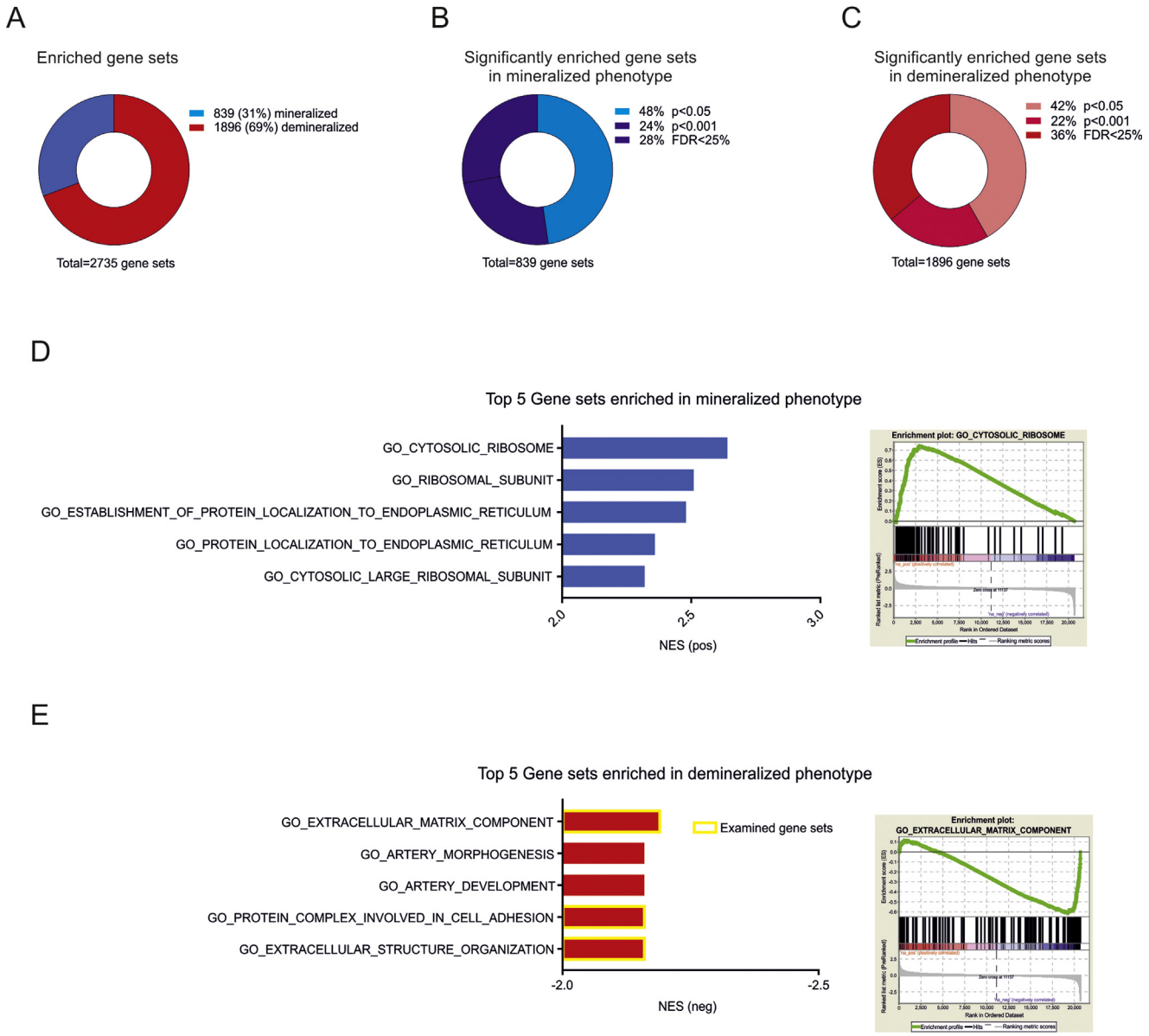

Fig. 4. *The matrix mineralization state independently regulates osteoblastic gene expression.* (**A**) Enriched Gene Sets on mineralized (blue) and demineralized (red) bone surfaces. (**B** and **C**) Distribution of statistical significance within enriched gene sets on mineralized (**B**) and demineralized (**C**) bone surfaces, considering p-value and false-discovery-rate (FDR). (**D** and **E**) Plotted top five enriched gene sets on mineralized (**D**) and demineralized (**E**) bone surfaces with displayed NES and GSEA Enrichment Plot of gene set with highest achieved NES. Osteoblastic cells on mineralized surfaces exclusively enriched genes sets linked to protein synthesis. In contrast, on the demineralized surfaces three of the five enriched gene sets were associated with the matrix. Gene sets marked with a yellow boarder were associated with the extracellular matrix and further investigated.

characteristic of our model as it offers highest in vitro relevance to in vivo biology. We have shown here that exposure to PAA, which has been previously used to sterilize bone samples [20], with or without prior standard histological decalcification with EDTA resulted in demineralized or mineralized bone tissue surface suitable for subsequent cell culture. Importantly, demineralization of the surface did not result in any detectable molecular changes to the osseous surface other than the depletion of mineral. With respect to EDTA, this observation is in line with reported data showing preservation of the organic portion of the matrix post EDTA treatment [21]. We believe that the molecular characterization of osseous surface models provides an important benchmark for studies addressing the interaction of bone cells with osseous surfaces. Although limited in scope, our findings indicated that PAA exposure, at least on the mineralized surface, did not result is major alterations when compared to reference bone. Another characteristic of the presented surface model is the ability to efficiently recover cells from the surface using a standard cell lifter. This feature is important as it allows for subsequent molecular analysis of the surface cells with minimal or no interference with the bone substrate itself. It is a particular strength of the presented surface model that it can be expanded and adapted in several important aspects. For example, the study described used porcine bone due to its availability, but human bone could be used seemingly instead. Also, the chelate-based decalcification should permit gradual demineralization of the surface, thus allowing experiments beyond the binary mineralization state, i.e. mineralized and demineralized, used in this study. Further, as we designed the model with future imaging applications in mind, it is likely that it can be adapted to fluorescence-based time-lapse microscopy studies of, for example, osteoblast motility. This would be important because upon attachment, migration of osteoblasts on the surface is expected [22], and from the results described here it is likely that osteoblasts exhibit a different migratory response to mineralized and demineralized

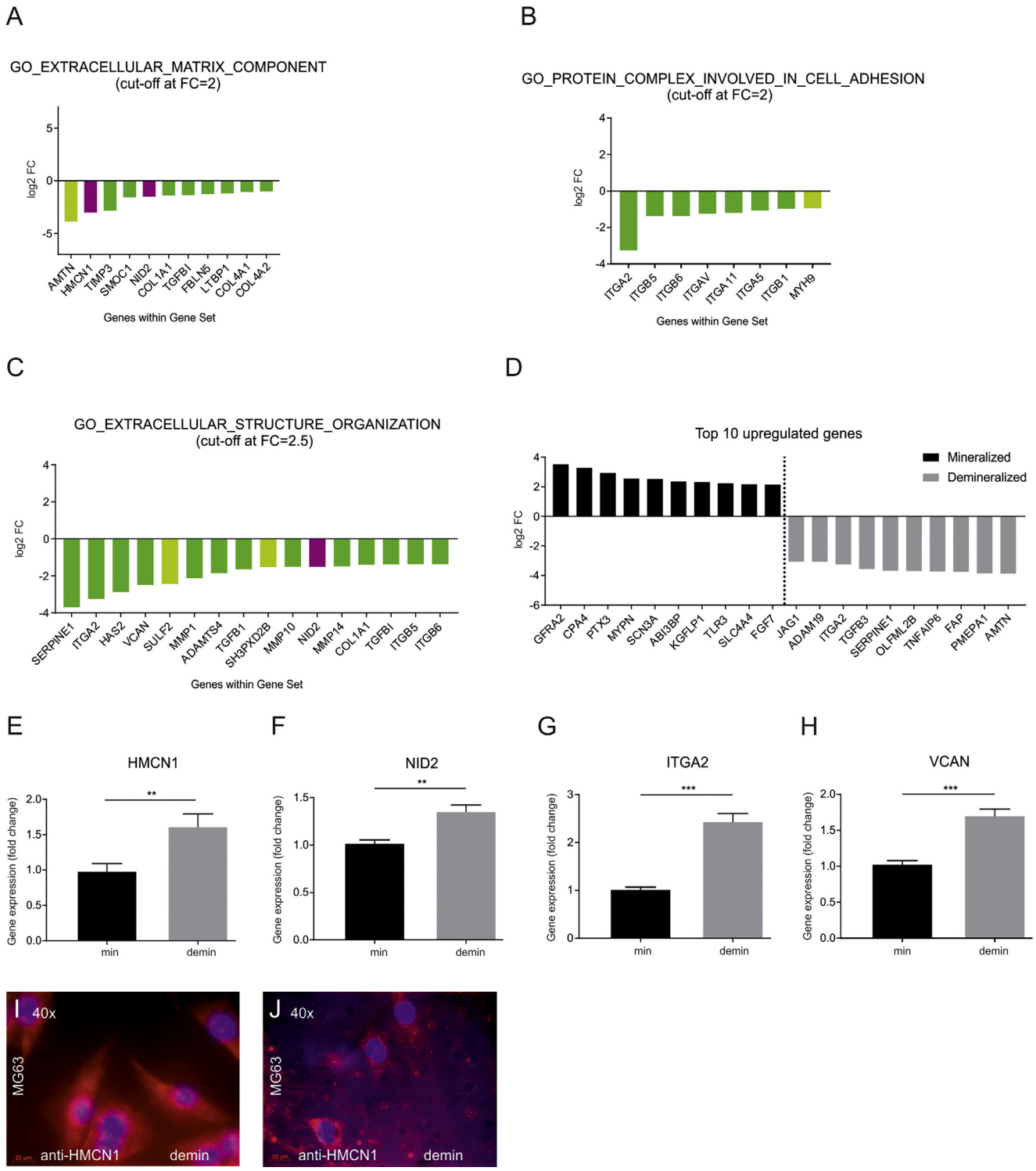

Fig. 5. *Identification of HMCN1 and NID2*. (**A–C**) Detailed plots of examined gene sets and comprising genes enriched on demineralized bone surfaces. Genes within shown gene sets are ranked by measured log2 FC and defined cut-off. Differentially expressed genes are color-marked, depicting a well-established (dark green), a less-reported (light green) and a currently not known (purple) function in osteoblasts. (**D**) Top 10 upregulated genes on mineralized and demineralized bone surfaces. (**E–H**) QRTPCR results with measured fold-changes of relative gene expression between mineralized and demineralized bone surfaces. Relative gene expression of mineralized bone surfaces was set to one, serving as reference. Means with standard deviation are shown. Significance was denoted as $^{**}p < 0.01$ and $^{***}p < 0.001$. (**G** and **H**) Immunofluorescence staining for HMCN1 (red channel) on MG63 cells seeded onto demineralized bone surface. Cell nuclei were co-stained with DAPI (blue channel). Abbreviations: demin, demineralized; min, mineralized.

surfaces. Moreover, the presented model is not limited to MG63 cells. It should be compatible not only with other types of osteoblastic cells, but also cell types expected to closely interact with osteoblasts, such as osteoclasts or vascular endothelial cells or even bone lining cells. We primarily utilized MG63 cells in this study because they (a) share many cellular and molecular characteristics of osteoblasts, (b) are widely used as osteoblast model, and (c) permit timely generation of reproducible cell numbers [23]. However, it is important to exercise caution when

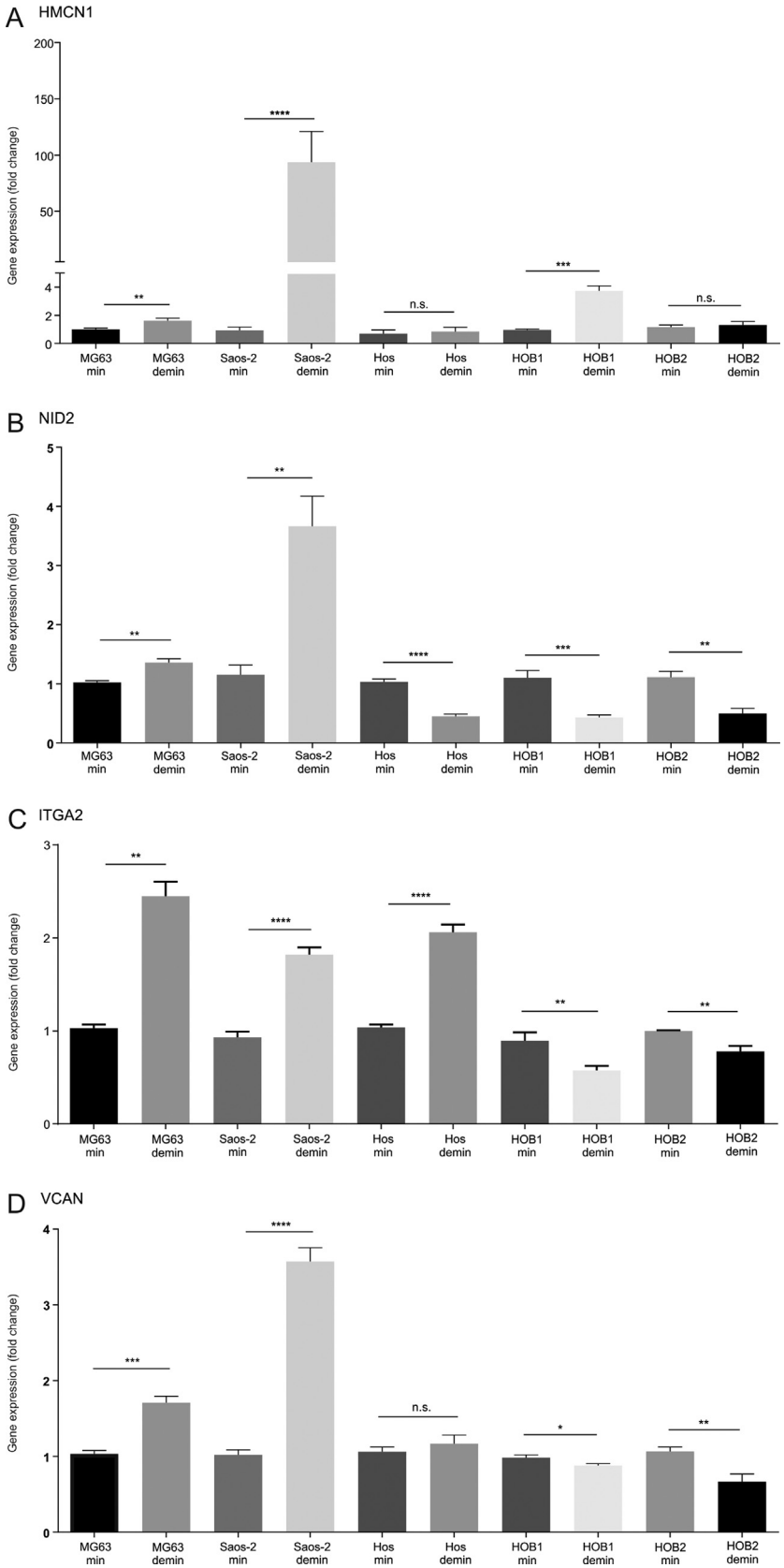

Fig. 6. *Cross-validation of HMCN1 and NID2 expression in different transformed and primary osteoblasts.* (**A–D**) QRTPCR results with measured fold-changes of relative gene expression between mineralized and demineralized bone surfaces. Relative gene expression of mineralized bone surfaces was set to 1, serving as reference. Means with standard deviation are shown. Significance was denoted as *p < 0.05, **p < 0.01, ***p < 0.001, ****p < 0.0001. Abbreviations: demin, demineralized; min, mineralized; n.s., not significant.

interpreting results from MG63 studies, as they are transformed cells derived from an osteosarcoma patient and hence cannot fully recapitulate true osteoblast biology. As the surface model can accommodate various cells types, we cross-validated our findings on a panel of transformed and primary osteoblasts. As expected we observed some degree of variation among the cell types, however we stress the value of such panels as they help to better define the role of genes in osteoblast populations.

Application of the surface model permitted isolation and subsequent gene expression analysis of osteoblastic cells residing on mineralized and demineralized surfaces. To our knowledge such an analysis has not been reported before. However, previous work has profiled gene expression of osteoblasts on orthopedic and dental biomaterials, in particular heavily processed, granulated bone mineral or matrix, providing insight into up and down-regulated genes on individual, exogenous materials [24–28].

The GSEA data presented here demonstrated in osteoblasts on mineralized surfaces principle enrichment of genes sets related to the formation of the ribosome and to the guidance of proteins to a specific location within the ER. This observation was unexpected and is potentially of interest, as very little is known about the response of osteoblasts to mineralized surfaces. Both the ribosome and ER are essential parts of the cellular protein production machinery. Given that mature osteoblasts have a high capacity for protein production, our finding suggests that osteoblasts on mineralized surfaces prime for subsequent protein production. To this end, it would be tempting to compare gene expression in osteoblast and bone lining cells on mineralized surfaces. In comparison to the mineralized surface, no significant enrichment of ribosomal and ER-related gene sets was observed in osteoblastic cells on the demineralized bone. The top ranking gene sets on this surface were associated primarily with bone matrix assembly and vascular response. Intriguingly, the observed upregulation of genes was a sole function of the matrix mineralization state. Consequently, it is likely that osteoblasts directly process the signals provided by the surface to control gene expression or they possibly engage a growth factor or cytokine based autocrine response. With respect to the vascular gene sets, this observation is not fully unexpected as the tight coupling of osteogenesis and angiogenesis has been well described [29,30]. Another finding in our study is the up-regulation of HMCN1 (hermicentin-1/fibulin-6) and NID2 (nidogen-2) in osteoblastic cells in response to the demineralized surface. Both gene products code for matrix glycoproteins and were previously not reported to play a role in osteoblasts. While HMCN1 plays an important role in extracellular adhesion, formation of cell-cell and cell-basement membrane adhesions that hold cells together, and maintenance of tissue and organ integrity [31,32], NID2 has established type 1 collagen binding capacity and functions as selective adhesion substrate for cells [33,34]. Supporting a role of NID2 in osteoblast function is data by Böse et al. showing skeletal forelimb abnormalities in about 15% of NID1/2 double knock out mice [35]. These data on HMCN1 and NID2, although derived from tissues other than bone, make it likely that these proteins act as attachment and migration guides for osteoblasts. Thus, it will be of considerable interest to assess the exact function of HMCN1 and NID2 in osteoblasts in subsequent studies. Lastly, the osseous surfaces that we began to model in this study not only play a role in normal bone physiology but also bone pathologies and injuries. For example, osteoporosis manifests primarily at sites of bone remodeling, i.e. the BMU. We speculate that the BMU has a unique make up of osseous surfaces, which may have potential for therapeutic intervention. Notably, bisphosphonates, a clinically successful class of osteoporosis drugs, exert an effect on bone cells via targeting to the osseous surface. Thus, delineating the interaction between osseous surfaces and the skeletal cells residing on them may offer new opportunities for targeted therapy of defined bone cell populations. Another example of a tissue characterized by multiple osseous surfaces is the fracture repair site. Its surface composition of resorbed bone, various collagen matrices, osteoid, woven or lamellar bone, may present osseous targets for intervention, for example in patients with compromised fracture healing. Together, understanding the interplay of osseous surfaces and bone cell behavior is important not only to understand normal bone physiology but also to devise novel therapeutic strategies for bone diseases.

Acknowledgements

This work was funded by the German Research Foundation (DFG) Grant MA 2188/5-1 to PMK. The National Institutes of Health (NIH) Grants R01 AR056145 and NIH R21 AR071704 (both to NP) supported this study. GR, vER and OS (2009.109.3) received funding from the Wilhelm Sander Foundation. The authors are indebted to Dr. Jonatan Darr for his invaluable help with the fluorescence microscopy.

Appendix A. Supplementary material

Supplementary data associated with this article can be found in the online version at doi:10.1016/j.yexcr.2018.09.005.

References

[1] F. Long, Building strong bones: molecular regulation of the osteoblast lineage, Nat. Rev. Mol. Cell Biol. 13 (2011) 27–38.
[2] I. Matic, B.G. Matthews, X. Wang, N.A. Dyment, D.L. Worthley, D.W. Rowe, D. Grcevic, I. Kalajzic, Quiescent bone lining cells are a major source of osteoblasts during adulthood, Stem Cells 34 (2016) 2930–2942.
[3] F.F. Safadi, M.F. Barbe, S.M. Abdelmagid, M.C. Rico, R.A. Aswad, J. Litvin, S.N. Popoff, Bone structure, development and bone biology, in: J.S. Khurana (Ed.), Bone Pathology, Humana Press, 2009.
[4] B.D. Boyan, Z. Schwartz, A.L. Boskey, The importance of mineral in bone and mineral research, Bone 27 (2000) 341–342.
[5] A.L. Boskey, Biomineralization: an overview, Connect Tissue Res. 44 (Suppl. 1) (2003) S5–S9.
[6] T. Hassenkam, G.E. Fantner, J.A. Cutroni, J.C. Weaver, D.E. Morse, P.K. Hansma, High-resolution AFM imaging of intact and fractured trabecular bone, Bone 35 (2004) 4–10.
[7] M.H. Helfrich, G. Stenbeck, S.A. Nesbitt, M.A. Horton, Integrins and other cell surface attachment molecules of bone cells, in: J.P. Bilezikian, L.G. Raisz, T.J. Martin (Eds.), Principles of Bone Biology, 1 Academic Press, San Diego, 2008, pp. 385–424.
[8] S. Gronthos, K. Stewart, S.E. Graves, S. Hay, P.J. Simmons, Integrin expression and function on human osteoblast-like cells, J. Bone Miner. Res. 12 (1997) 1189–1197.
[9] D.E. Hughes, D.M. Salter, S. Dedhar, R. Simpson, Integrin expression in human bone, J. Bone Miner. Res. 8 (1993) 527–533.
[10] D. Zimmerman, F. Jin, P. Leboy, S. Hardy, C. Damsky, Impaired bone formation in transgenic mice resulting from altered integrin function in osteoblasts, Dev. Biol. 220 (2000) 2–15.
[11] D. Bouvard, A. Aszodi, G. Kostka, M.R. Block, C. Albiges-Rizo, R. Fassler, Defective osteoblast function in ICAP-1-deficient mice, Development 134 (2007) 2615–2625.
[12] T. Sotobori, T. Ueda, A. Myoui, K. Yoshioka, M. Nakasaki, H. Yoshikawa, K. Itoh, Bone morphogenetic protein-2 promotes the haptotactic migration of murine osteoblastic and osteosarcoma cells by enhancing incorporation of integrin beta1 into lipid rafts, Exp. Cell Res. 312 (2006) 3927–3938.
[13] P.J. Marie, Targeting integrins to promote bone formation and repair, Nat. Rev. Endocrinol. 9 (2013) 288–295.
[14] A. Boskey, N. Pleshko Camacho, FT-IR imaging of native and tissue-engineered bone and cartilage, Biomaterials 28 (2007) 2465–2478.
[15] R.S. Thomas, P.D. Mitchell, R.O. Oreffo, H. Morgan, Trapping single human osteoblast-like cells from a heterogeneous population using a dielectrophoretic microfluidic device, Biomicrofluidics 4 (2010).
[16] A. Subramanian, P. Tamayo, V.K. Mootha, S. Mukherjee, B.L. Ebert, M.A. Gillette, A. Paulovich, S.L. Pomeroy, T.R. Golub, E.S. Lander, J.P. Mesirov, Gene set enrichment analysis: a knowledge-based approach for interpreting genome-wide expression profiles, Proc. Natl. Acad. Sci. USA 102 (2005) 15545–15550.
[17] A. Liberzon, A. Subramanian, R. Pinchback, H. Thorvaldsdottir, P. Tamayo, J.P. Mesirov, Molecular signatures database (MSigDB) 3.0, Bioinformatics 27 (2011) 1739–1740.
[18] M. Shemesh, S. Addadi, Y. Milstein, B. Geiger, L. Addadi, Study of osteoclast adhesion to cortical bone surfaces: a correlative microscopy approach for concomitant imaging of cellular dynamics and surface modifications, ACS Appl. Mater. Interfaces 8 (2016) 14932–14943.
[19] M.A. Karsdal, M.S. Fjording, N.T. Foged, J.M. Delaisse, A. Lochter, Transforming growth factor-beta-induced osteoblast elongation regulates osteoclastic bone resorption through a p38 mitogen-activated protein kinase- and matrix metalloproteinase-dependent pathway, J. Biol. Chem. 276 (2001) 39350–39358.
[20] A. Pruss, B. Baumann, M. Seibold, M. Kao, K. Tintelnot, R. von Versen, H. Radtke, T. Dorner, G. Pauli, U.B. Gobel, Validation of the sterilization procedure of allogeneic avital bone transplants using peracetic acid-ethanol, Biologicals 29 (2001)

59–66.
[21] A.A. Abrantes, A. Rafacho, E.R. Rivero, F.V. Mariano, F.M. Siqueira, R.O. Gondak, Tissue integrity, costs and time associated with different agents for histological bone preparation, Microsc. Res. Tech. 80 (2017) 344–349.
[22] A. Thiel, M.K. Reumann, A. Boskey, J. Wischmann, R. von Eisenhart-Rothe, P. Mayer-Kuckuk, Osteoblast migration in vertebrate bone, Biol. Rev. Camb. Philos. Soc. 93 (2018) 350–363.
[23] E.M. Czekanska, M.J. Stoddart, R.G. Richards, J.S. Hayes, In search of an osteoblast cell model for in vitro research, Eur. Cell Mater. 24 (2012) 1–17.
[24] R.J. Miron, D.D. Bosshardt, Y. Zhang, D. Buser, A. Sculean, Gene array of primary human osteoblasts exposed to enamel matrix derivative in combination with a natural bone mineral, Clin. Oral Investig. 17 (2013) 405–410.
[25] F. Carinci, A. Piattelli, M. Degidi, A. Palmieri, V. Perrotti, L. Scapoli, M. Martinelli, G. Laino, F. Pezzetti, Genetic effects of anorganic bovine bone (Bio-Oss) on osteoblast-like MG63 cells, Arch. Oral Biol. 51 (2006) 154–163.
[26] F. Carinci, A. Piattelli, M. Degidi, A. Palmieri, V. Perrotti, L. Scapoli, M. Martinelli, L. Zuccarino, F. Pezzetti, Effects of demineralized freeze-dried bone allograft on gene expression of osteoblastlike MG63 cells, Int. J. Periodontics Restor. Dent. 27 (2007) 596–601.
[27] N. Yamamichi, K. Pugdee, W.J. Chang, S.Y. Lee, M. Yoshinari, T. Hayakawa, Y. Abiko, Gene expression monitoring in osteoblasts on titanium coated with fibronectin-derived peptide, Dent. Mater. J. 27 (2008) 744–750.
[28] K. Pugdee, Y. Shibata, N. Yamamichi, H. Tsutsumi, M. Yoshinari, Y. Abiko, T. Hayakawa, Gene expression of MC3T3-E1 cells on fibronectin-immobilized titanium using tresyl chloride activation technique, Dent. Mater. J. 26 (2007) 647–655.
[29] E. Schipani, C. Maes, G. Carmeliet, G.L. Semenza, Regulation of osteogenesis-angiogenesis coupling by HIFs and VEGF, J. Bone Miner. Res. 24 (2009) 1347–1353.
[30] A. Grosso, M.G. Burger, A. Lunger, D.J. Schaefer, A. Banfi, N. Di Maggio, It takes two to tango: coupling of angiogenesis and osteogenesis for bone regeneration, Front. Bioeng. Biotechnol. 5 (2017) 68.
[31] B.E. Vogel, E.M. Hedgecock, Hemicentin, a conserved extracellular member of the immunoglobulin superfamily, organizes epithelial and other cell attachments into oriented line-shaped junctions, Development 128 (2001) 883–894.
[32] X. Xu, M. Xu, X. Zhou, O.B. Jones, E. Moharomd, Y. Pan, G. Yan, D.D. Anthony, W.B. Isaacs, Specific structure and unique function define the hemicentin, Cell Biosci. 3 (2013) 27.
[33] E. Kohfeldt, T. Sasaki, W. Gohring, R. Timpl, Nidogen-2: a new basement membrane protein with diverse binding properties, J. Mol. Biol. 282 (1998) 99–109.
[34] M.S. Ho, K. Bose, S. Mokkapati, R. Nischt, N. Smyth, Nidogens-extracellular matrix linker molecules, Microsc. Res. Tech. 71 (2008) 387–395.
[35] K. Bose, R. Nischt, A. Page, B.L. Bader, M. Paulsson, N. Smyth, Loss of nidogen-1 and -2 results in syndactyly and changes in limb development, J. Biol. Chem. 281 (2006) 39620–39629.